Selective Voronoi Tessellation as a Method to Design Anisotropic and Biomimetic Implants

Joseph Deering[1,†], Kierdra I. Dowling[1,†], Liza-Anastasia DiCecco[1], Griffin D. McLean[2], Bosco Yu[1], Kathryn Grandfield[1,3*]

[†] These authors contributed equally.

[1] Department of Materials Science and Engineering, McMaster University, Hamilton, ON, Canada
[2] Department of Mechanical Engineering, McMaster University, Hamilton, ON, Canada
[3] School of Biomedical Engineering, McMaster University, Hamilton, ON, Canada

[*] Corresponding author:
       Prof. Kathryn Grandfield
       McMaster University
       1280 Main Street West
       Hamilton, ON, L8S 4L7
   Canada
       Email: kgrandfield@mcmaster.ca

Abstract

The geometry of a metallic scaffold is important for the success of bone implants, where the introduction of porosity can reduce stress shielding effects and allow for bone tissue integration. In this work, porous scaffolds were designed to closely mimic the natural structure of trabecular bone using selective Voronoi tessellation with preferential seeding. A workflow to generate these structures is introduced, where voided regions of seeds in the starting volume create preferential texture during polyhedral expansion, resulting in modified strut orientation in the implant. Anisotropy was digitally characterized by mean-intercept length and star volume distribution measurements to determine similarity to trabecular orientation. This work demonstrates that selective Voronoi tessellation is an effective method to generate biomimetic porous scaffolds with increased anisotropy and tunable strut architecture in three dimensions as a suitable alternative to patient-derived bone geometries.

Keywords
Implant design, Biomimetics, Bone implants, Osseointegration, Additive manufacturing

Graphical Abstract
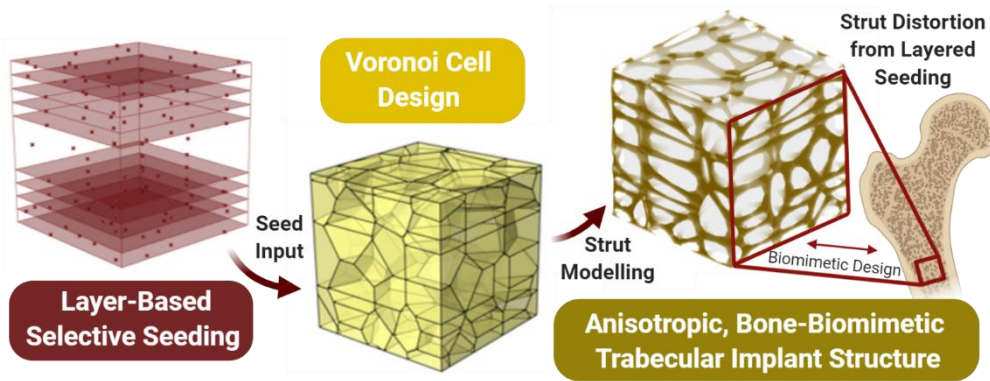

1. Introduction

Stress shielding is a phenomenon that occurs when a high-stiffness implant in the human body results in bone loss. Decreased physiological loading occurs in the bone due to a stiffness mismatch between the implant and the surrounding bone, causing a reduction in bone density [1] and higher likelihood of periprosthetic fracture [2]. Stiffness reduction by material selection [3,4] or by intentional introduction of porosity into the implant structure [5–7] are two possible strategies to mitigate this effect. Introducing porosity into the structure not only reduces stress shielding effects, but also facilitates tissue ingrowth [8]. Geometric factors of a porous metallic implant such as pore size [9] and pore geometry [10] have been found to influence osseointegration. To date, there is no well-defined set of geometric parameters for optimal osseointegration in porous metallic implants, but it is believed that biomimetic pore structures may outperform other implant geometries.

Trabecular bone is a naturally anisotropic network of struts and plates [11]. The inter-trabecular angle (ITA) measures the angle at trabecular junctions and has been shown to be based on the trabecular geometry [11]. The ITA distribution of nodes with 3 connecting trabeculae (3N junctions) have a mean close to $120°$, nodes with 4 connecting trabeculae (4N junctions) have a mean close to $109°$ and nodes of higher connectivity (5N, 6N, or higher junctions) have mean ITA values around $100°$ [11]. These trabecular struts reflect loading conditions and are found to be co-oriented or offset by a fixed amount from the mechanical axis of the bone [12]. The bulk of traditional implants do not take anisotropy into account, where fully dense materials or porous isotropic implants are predominant [13]. Some biomimetic approaches use voxel-based finite element modelling of human trabeculae as observed by X-ray micro-computed tomography [14] to exactly mimic human trabeculae [15]. This is often limited by high cost or intensive computation. Since the global trabecular orientation lines up with the major axis of mechanical loading in the bone [16], it is desirable to produce scaffolds that have struts elongated in this direction. Scaffolds like these can be translated to implants in a clinical setting for total hip joint replacements or arthroplasty which involves replacement of femoral bone, for example, where the cortical bone displays overall orthotropy and increased anisotropy close to the epiphyses [17] and the trabeculae have preferred orientation along several tension/compression lines in the proximal femur [18].

It is well-known that there is a significant correlation between the mechanical axis of bone and the trabecular orientation, especially in the long bones [12], where the direction of force transmitted through the bone varies along the mechanical axis [12]. The mechanical axis of the lower extremity typically refers to the line drawn from the center of the femoral head down to the center of the ankle joint [19]. On average, this is found to have a global 3° offset from the vertical axis [20]. The mechanical axis can then be separated into two separate subdivisions, the femoral mechanical axis and the tibial mechanical axis [19]. The femoral mechanical axis extends from the head of the femur to the intercondylar notch of the distal femur, whereas the tibial mechanical axis runs from the center of the proximal tibia to the center of the ankle [20]. In the average healthy human, the mechanical tibiofemoral angle is slightly higher than 180°, however this can range case by case. One study found that the average mechanical tibiofemoral angle ranged from 183-186° [21], varying widely based on the patient's height, pelvic width, sex, and age [22]. These linear approximations of the mechanical axis are somewhat limited in scope, especially considering how local regions of the bone can vary within these axes. Due to the offset loading condition associated with a local mechanical axis and inherent curvature around the femoral metaphysis, consideration with respect to implant design are complex. Global alignment of porous implant struts to the mechanical axis can be achieved with unidirectionally oriented repeating structures but a closer look at the anisotropy of the native bone proves this to be unsuitable.

Voronoi tessellation has been previously used to develop metallic scaffolds with a randomized pore architecture [23]. A Voronoi tessellation is generated as shown in Figure 1. First, seeds are placed in a finite space from which a polygon or polyhedron grows outward, expanding at a constant rate to fill a space. Growth finishes when neighbouring polyhedra impinge on one another [23]. In a three-dimensional space, these boundaries consist of planes rather than lines. By forming solid struts out of the polyhedral junctions, scaffolds can be created with a trabecular appearance at the microscale [24] but an isotropic mechanical behaviour at the macroscale, as has been shown in 2D Voronoi tessellations [25]. The mechanical benefits of cellular Voronoi structures have been investigated previously, where change to the isotropy of the cellular structure can affect the deformation mode and stiffness of the structure [26]. Two-dimensional Voronoi honeycombs with a high degree of regularity have been shown to behave isotropically in mechanical deformation, where introducing disorder to the structure can result in a change of the Young's modulus [27]. Similarly, random strut defects have been observed to affect the elastic moduli [28], displaying particular dependence on the main deformation mode of the unit cell [29]. Introduction of crystal-inspired randomness to the macroscale hierarchy of an otherwise repeating strut configuration offers the potential for refinement of mechanical properties [30]. To produce biomimetic implants with tunable mechanical properties, adjustment to the conventional modelling of cellular Voronoi structures is required to generate structural anisotropy and control the mechanical response of the implant, thereby modulating bone regeneration.
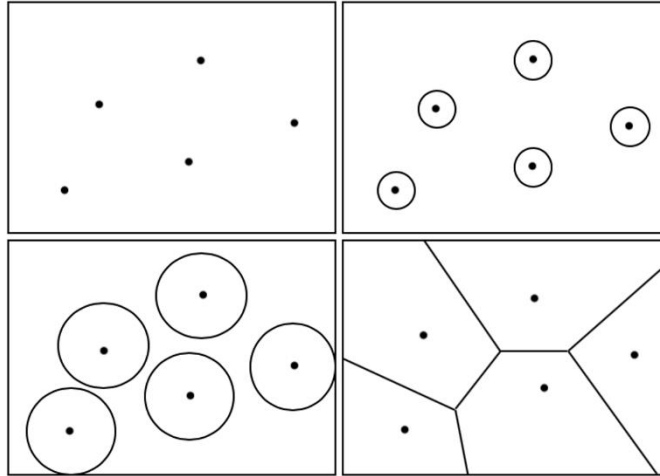
Figure 1: Graphical representation showing the formation of a Voronoi diagram in 2D. Seeds are randomly distributed through a region, grow outward until they impinge on one another, and form distinct polygons.

Producing implants with such complex geometries is often unachievable by traditional manufacturing techniques. However additive manufacturing (AM) can produce complex and intricate implants with limited post-processing steps [31]. This technique deposits material layer-by-layer, allowing the formation of complex structures with internal pore architectures that cannot be replicated in traditional subtractive technologies [31]. By using an additive, layer-by-layer approach to selectively deposit material [32], AM is not burdened by the same limitations concerning internal pore architecture that govern traditional subtractive technologies [33]. For example, selective laser melting (SLM) is able to produce structures with thin walls and hidden voids or channels [34]. Complex structures, such as rhombic dodecahedral honeycomb lattices [35], weighted planar stochastic lattices [35], and implants based off patient geometry [22] have also been fabricated with SLM. The *in vitro* performance of SLM scaffolds designed with a standard Voronoi tessellation showed that the trabecular-like porous structure exhibited enhanced cell proliferation and osteoblast differentiation compared to structures with fewer irregularities and repeating patterns [36]. This suggests that SLM is a suitable manufacturing process for production of porous lattices designed by any form of Voronoi tessellation in the future, and that these structures may also perform favorably in *in vitro* and *in vivo* environments.

In this study, we report the development of biomimetic and anisotropic porous scaffolds by a new method, selective Voronoi tessellation, and quantify the anisotropy and select histomorphometry of the resulting structures. This new method of designing porous trabecular structures has implications with regards to both osseointegration and mechanical load distribution in the design of porous anisotropic implants for joint replacement, in particular, for the application of total hip arthroplasty.

2. Methods

2.1. Voronoi Tessellation

Rhinoceros3D 6 (Robert McNeel & Associates) with the Grasshopper graphical programming add-on was used to model both simple isotropic and anisotropic implant models by Voronoi tessellation, as described in work from Fantini and Curto [37]. Four bounding points and the associated curves were lofted to create a cubic geometry of 6 mm x 6 mm x 6 mm for both the isotropic and anisotropic structures. The complete Grasshopper scripts can be found in supplemental information, where the workflows for each are documented in Figure 2 and additional steps for selective seeding are highlighted in purple.
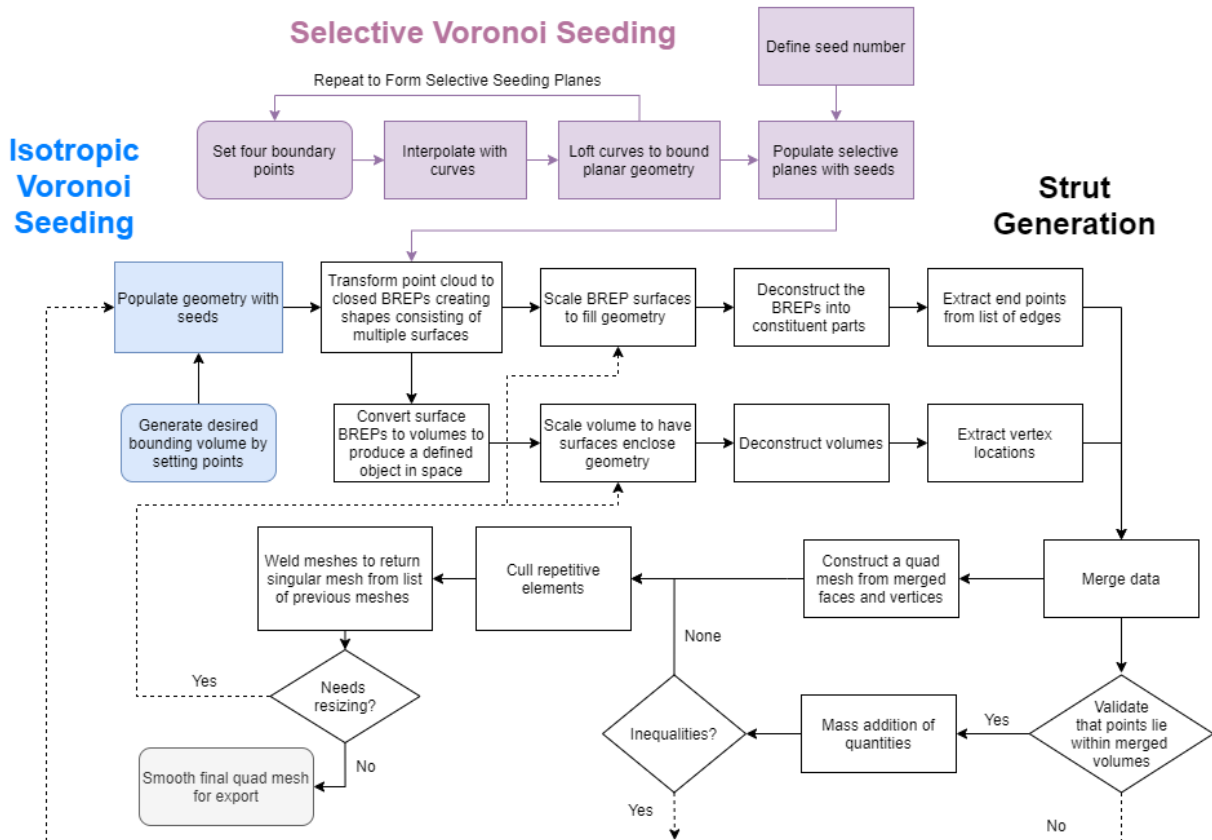

Figure 2: Flow chart detailing the generation of standard Voronoi tessellations and selective Voronoi tessellations (purple extension) in Grasshopper to make implant structures. The selective seeding algorithm creates biomimetic anisotropy in the final structure.

For the isotropic implant, dynamic seed population control was added using a numerical slider. One hundred and twenty-three seeds were randomly distributed through the volume and converted to boundary representations (BREPs) containing locations of vertices, edges, and faces for each volume. The BREPs were simultaneously transformed into bound volumes and scaled down to fit within the bounding cube, effectively creating a polyhedron from each seed. Volume endpoints for each polyhedron were extracted from both BREPs and volumes to get spatial coordinates for vertices in each polyhedron in one continuous object. Scaffold struts were formed along volume edges connecting these vertices and converted to independent meshes for each strut. Repetitive or overlapping mesh elements were culled before all meshes were welded to a single mesh to compose the penultimate Voronoi tessellation in 3D. The relative size of struts in the tessellation was assessed qualitatively to iteratively select an appropriate scaling factor for the constituent

BREPs and volumes. A recursive Catmull-Clark subdivision algorithm was used to smooth the final mesh after scaling and remove any mesh errors.

The three anisotropic implants used selective Voronoi tessellation by a controlled distribution of seeds to form strut directionality. Anisotropic implants were generated by controlled redistribution of seeds into periodic planes in the upper and lower third of the cube. For this, five equally spaced cross-sectional planes with an interplanar spacing of 0.5 mm were bound at the top as well as at the bottom of the cube. For the three models, ranges of 3-5, 5-7, and 8-10 seeds per plane (SPP) were considered for each, respectively. To have the same amount of seeds per volume considered (totalling to 123), the total number of SPP in a model was subtracted from 123 and these remaining non-planar seeds were evenly distributed throughout the 6 mm x 6 mm x 6 mm volume and the workflow was resumed in the described manner for the isotropic implant.

2.2. Strut Analysis

Isotropic and anisotropic mesh files were exported to 500 voxel x 500 voxel x 500 voxel volumes in Autodesk Netfabb 2019 before being imported to Dragonfly 4.1 (Object Research Systems) as an image stack for analysis. Dragonfly's Bone Analysis tool was used to generate global measurements of mean-intercept length (MIL) and star volume distribution (SVD) [38,39] as a form of measuring anisotropy in all structures using 5,000 orientations and 10,000 iterations.

The MIL technique calculates the fabric tensor using the average distance between collinear points that lie on the periphery of segmented struts (L_{avg}), where varying angular orientations (ω) and a defined number of lines (m) are used to assign a final anisotropy value according to some scalar value as outlined in Equation 1 [40,41].

Equation 1 $MIL(\omega) = f\left(\frac{\sum_{i=1}^{m} L_{i,avg}(\omega)}{m}\right)$

The SVD technique also uses a fabric tensor, but the intercept length across a single strut (D) is instead found in several orientations for a single bounded point within the scaffold, where intercepts are then weighted in cubic fashion and averaged across a number of bounded points (n) as described in Equation 2. For further descriptions of the MIL and SVD techniques, we refer the reader elsewhere [41]. In cases of MIL and SVD measurements in this study, a higher value of MIL or SVD refers to a greater degree of anisotropy in the trabecular structure. Therefore, when MIL or SVD = 0, this refers to an isotropic structure, and when MIL or SVD approaches 1, the degree of anisotropy increases.

Equation 2 $SVD(\omega) = f\left(\frac{\sum_{i=i}^{n} D_i(\omega)^3}{n}\right)$

The bone volume fraction (BV/TV) and mean trabecular thickness (Tb.Th) for each structure were also assessed using the Bone Analysis tool in Dragonfly. Representative vector fields were also generated as colorimetric descriptors of strut orientation using the surface-normal algorithm for each implant using the projection tool in Dragonfly with sample spacing of 94 µm. Vectors parallel to the defined X-axis appear red, vectors parallel to the Y-axis appear green, vectors parallel to the

Z-axis appear blue, and intermediate vectors are assigned a corresponding colour based on their misorientation with respect to the coordinate axes.

Image stacks were also imported into ImageJ (NIH) for ITA pre-processing. Image stacks were skeletonized across the 3D volume and branch information, including vector endpoints, was exported. A list of unique vector endpoints was filtered from the branch information and the number of vectors sharing a particular endpoint was used to define the junction type (3N, 4N, 5N, or other). Vectors were loaded into a custom script in R 3.6.1 for the measurement of ITAs in each junction type.

3. Results

3.1. Voronoi Tessellation

The seed distribution for isotropic and anisotropic structures is shown in Figure 3. As anticipated, the anisotropic structures contain regions with higher seed density near the planar additions and regions with lower seed density in the voided regions. Seeding in the isotropic structure appears random, but uniform in comparison to the anisotropic structures. Upon polyhedral expansion (Figure 4), preferential orientation was observed in the polyhedra of the anisotropic implants as a result of the heterogeneous seeding. Boundary conversion to lattice struts (Figure 5) visually confirms directionality in the anisotropic implants, where the meshed structures all have the appearance of naturally-occurring trabecular bone.
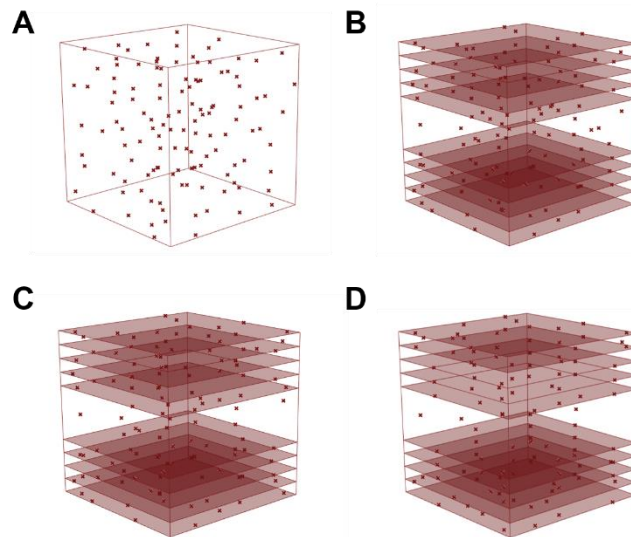
Figure 3: Selective Voronoi seeding in 6 mm x 6 mm x 6 mm cubic volumes. Anisotropic implants have seeds redistributed preferentially to the upper and lower thirds of the cube, but each cube contains 123 seeds. (A) Isotropic implant where seeding is entirely uniform. (B) Anisotropic implant with 3-5 seeds redistributed in each plane. (C) Anisotropic implant with 5-7 seeds redistributed in each plane. (D) Anisotropic implant with 8-10 seeds redistributed in each plane.
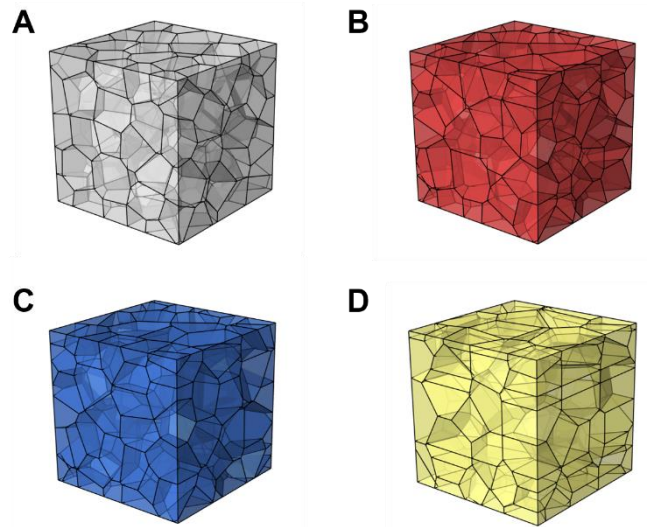
Figure 4: Polyhedral expansion in the isotropic and anisotropic implants. Polyhedral morphology appears uniform when using traditional Voronoi seeding and distorted when using selective Voronoi seeding. (A) Isotropic implant with uniform seeding. (B) Anisotropic implant with 3-5 seeds redistributed in each plane. (C) Anisotropic implant with 5-7 seeds redistributed in each plane. (D) Anisotropic implant with 8-10 seeds redistributed in each plane.

3.2. Strut Analysis

Normalized global anisotropy values by MIL and SVD measurements are shown in Table 1 for the isotropic and anisotropic implants. Adding the preferential seeding to form an anisotropic structure increased the MIL measurement in all cases relative to the isotropic structure. Increasing the number of seeds on each redistribution plane in the anisotropic structure also resulted in higher MIL, indicating a greater tendency for scaffold struts to be co-aligned in any anisotropic implant than the isotropic implant. A similar trend was observed for SVD measurements of anisotropy, where the anisotropic geometry with 8-10 seeds per plane had a substantially higher star volume distribution than any of the other implant models.
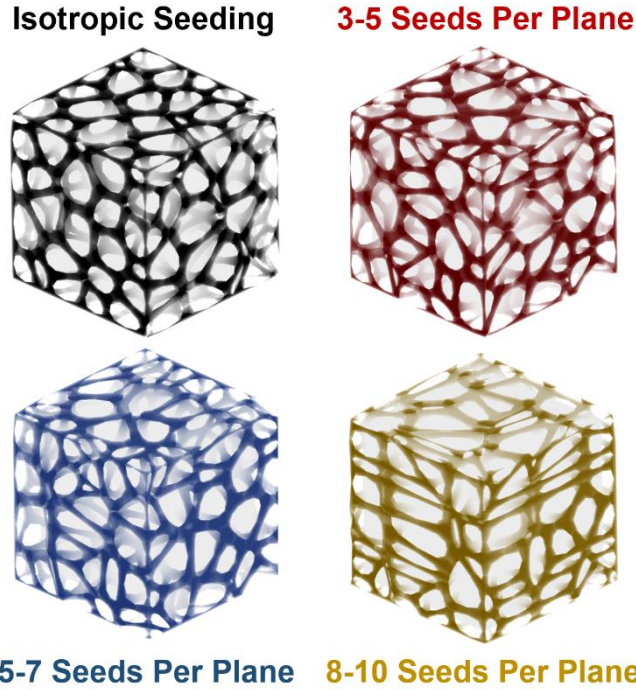
Figure 5: Resulting strut architecture of the isotropic implant (black), 3-5 SPP anisotropic implant (red), 5-7 SPP anisotropic implant (blue), and 8-10 SPP anisotropic implant (gold). As the number of seeds per plane increases, strut distortion is visible along two preferential axes.

Histomorphometry of each of the four structures is also shown in Table 1. For all four structures, the bone volume fraction was measured to be constant at 0.16. No appreciable deviation was observed in the trabecular thickness of struts generated using the isotropic or selective seeding techniques. For the isotropic structure and each of the preferentially seeded structures, the mean trabecular thickness ranged from 249 µm to 259 µm.

Table 1: Normalized degree of anisotropy for each implant. Nonuniform Voronoi seeding resulted in higher normalized values of anisotropy in the implant, which increased with increasing seed redistribution.

	Isotropic	3-5 SPP	5-7 SPP	8-10 SPP
Anisotropy (MIL)	0.06	0.11	0.21	0.38
Anisotropy (SVD)	0.16	0.14	0.18	0.34
Bone Volume Fraction (BV/TV)	0.16	0.16	0.16	0.16
Trabecular Thickness (Tb.Th)	258.7 µm	250.9 µm	251.2 µm	249.1 µm

The ITA measurements for each implant structure are shown in Figure 6, with average values and standard deviations reported in Table 2 alongside literature values from a human femur. For 3N junctions, the isotropic implant behaves very similarly to the anisotropic implants, where high-

angle inter-trabecular angles in the range of 130-170° are most abundant. Compared to tomography data averaged across a human femur [11], the deviation in mean 3N angle is within 5° for any of the implants investigated in this study.

4N junctions for the isotropic and anisotropic implants were also similar. Angles between 90-130° were most common for the Voronoi implant structures, which is lower than the values observed for the 3N junctions. While the mean 4N angle for the implants is slightly below that of an averaged human femur, the deviation is reduced to within 2-4° of human femoral tissue.

5N junctions were less common in the implants than 3N or 4N junctions, resulting in greater variation in the ITA plots. Similar to the 4N junctions, angles were commonly found in the range of 80-130°. No substantial difference was observed between the isotropic and anisotropic implant structures, where the deviation from human femoral tissue ranged from 2-3°.
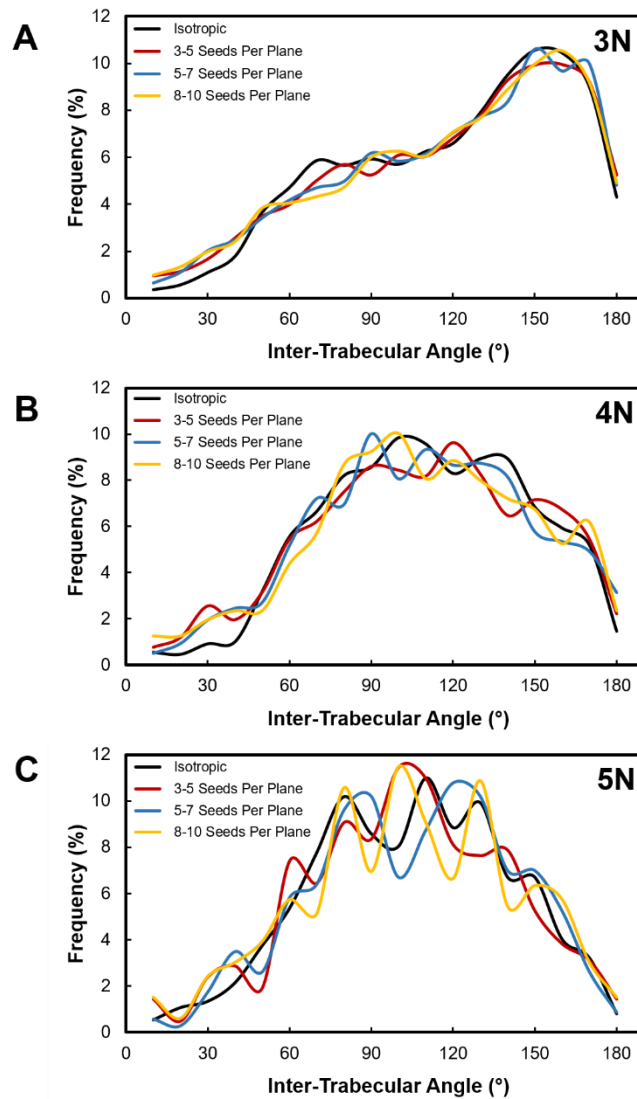

Figure 6: ITA measurements for isotropic, 3-5 SPP anisotropic, 5-7 SPP anisotropic, and 8-10 SPP anisotropic implants. (A) 3N junctions. High-angle ITAs (130-170°) are most frequent for

this junction type. (B) 4N junctions. ITAs in the range of 90-130° are more common in 4N junctions, where this range lies below that of the 3N junction type. (C) 5N junctions. ITAs are elevated in a somewhat similar range to that of 4N junctions (80-130°).

Table 2: Inter-trabecular angle measurements from the isotropic implant structure, anisotropic implant structure, and literature value for human femur. Values between test groups are similar for any given junction type.

	Isotropic	3-5 SPP	5-7 SPP	8-10 SPP	Human Femur
5N Junction	99.3° ± 35.9°	98.1° ± 37.3°	100.5° ± 36.3°	98.9° ± 38.6°	103.1° ± 33.0° [11]
4N Junction	105.3° ± 36.3°	103.5° ± 39.7°	103.5° ± 38.6°	103.3° ± 39.7°	107.6° ± 31.8° [11]
3N Junction	114.6° ± 40.7°	113.5° ± 42.9°	113.9° ± 42.7°	113.4° ± 43.2°	116.3° ± 29.1° [11]

Field vector diagrams (Figure 7) of the cube interior affirm these results. Vectors in this diagram are assigned a colour depending on co-alignment to a coordinate axis. In the isotropic implant, field vectors are distributed evenly between the three coordinate axes and their intermediate directions. In the anisotropic implants, especially in the 8-10 SPP implant, vectors are more likely to be co-oriented with the defined X-axis or Y-axis. Z-oriented vectors become less common as the seed redistribution is increased in an anisotropic Voronoi tessellation.

Isotropic Seeding   **3-5 SPP**   **5-7 SPP**   **8-10 SPP**
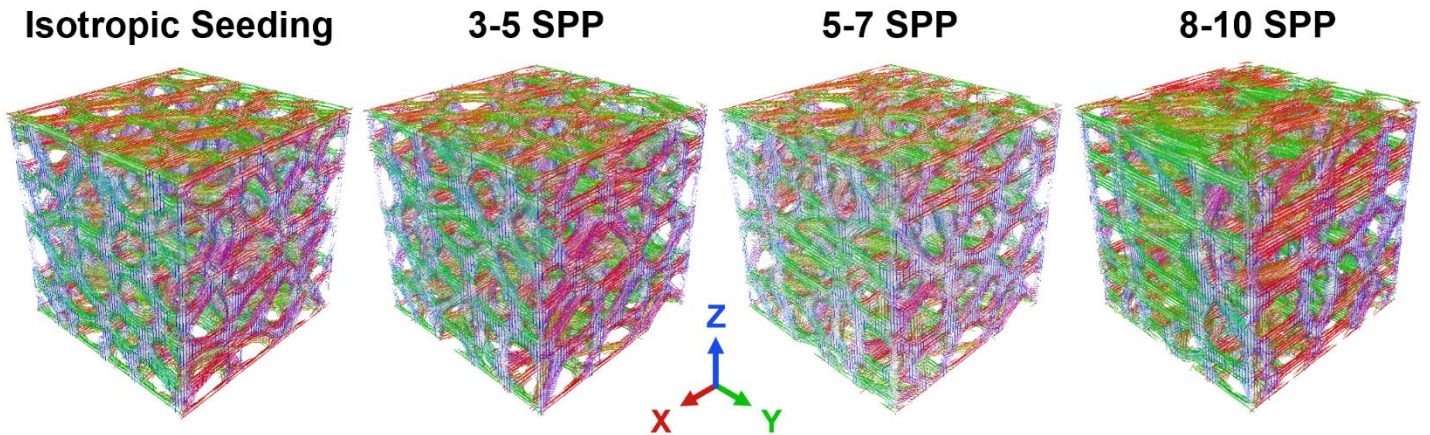
Figure 7: Field vector diagrams of the implant interior showing even distribution of field vectors in the isotropic implant versus the predominant alignment of field vectors in the X and Y axes for the anisotropic implants. Red vectors are aligned with the X-direction, green vectors are aligned with the Y-direction, and blue vectors are aligned with the Z-direction. Intermediate colours represent spatial orientation with respect to each coordinate axis. Blue vectors are notably less abundant in the 8-10 SPP implant.

4. Discussion

This work highlights a method of selective Voronoi tessellation as an effective means of creating a biomimetic anisotropic scaffold. By placing a higher density of Voronoi seeds in specific regions of the implant geometry, pores can be elongated in a desired direction. This elongation introduces anisotropy into the scaffold versus the traditional form of Voronoi tessellation, as measured by MIL.

The MIL anisotropy of the isotropic structure was found to be 0.06. This value is atypical of what is found in human femoral and humeral bone, which have been measured to average 0.641 and 0.207, respectively [42]. By introducing the redistributed seeding planes and adjusting their seed density, selective Voronoi tessellation was able to increase anisotropy to a range of 0.11-0.38 by MIL measurement, or up to 0.34 from 0.16 in the case of SVD measurement. The selective form of Voronoi tessellation for implant design is therefore able to better mimic human trabecular bone with regards to anisotropy by creating a customizable design environment. By adjusting the seed distribution in the implant geometry, implants can be designed with a target level of anisotropy that best matches the anatomy of the defect site. Similarly, bone volume fractions and trabecular thickness from isotropic and anisotropic Voronoi models were measured to be 0.16 and roughly 250 µm, respectively. These are both consistent with values from dual energy X-ray absorption scans of femoral trabecular bone in humans, where bone volume fractions are roughly 0.11 to 0.18 [43,44] and trabecular thickness can extend up to 250 µm [44]. The design of implants for joint replacement can make use of these biomimetic principles, where scaffold struts can be fabricated in an equivalent size to natural trabeculae in the defect site.

Trabecular bone geometry has also been stated to follow prescribed angles. Investigation of 5N/6N junctions in human femoral tissue shows angles most commonly between 80° and 115° [11]. This model is fairly consistent with an ideal trigonal bipyramidal structure, which contains six 90° angles and three 120° angles, for a mean ITA of 100°. A similar ITA distribution for 5N junctions was observed in the generation of the isotropic and anisotropic implants in this work, where the highest frequency of angles was in the range of 80-130° and mean 5N ITAs ranged from 98.1-100.5°. Similar observations can be made with the 4N junctions in the isotropic and anisotropic Voronoi implants, where the mean angle of 103.3-105.3° is comparable to a tetrahedral trabecular arrangement. In 3N junctions, the mean angle of 113.4-114.6° in the Voronoi tessellations suggests a possible similarity to a trigonal planar trabecular arrangement.

Here, our results were presented solely on the basis of a cubic volume. The cubic volume used for selective Voronoi tessellation is a model for a simplistic implant geometry, but the technique can certainly be expanded to other, more complex implant geometries. For example, future applications of this work could apply this selective tessellation to the design of complex geometrical implants. In one such potential extension of this work, looking at the femoral component of a typical total hip arthroplasty, the transition through the epiphyseal and metaphyseal regions typically follows the inherent curvature of the bone. The average angle between the femoral head and femur shaft in a healthy adult is approximately 130° [45]. While the global mechanical axis of the lower extremity runs at 3° [20], the average orientation of trabeculae in the epiphyseal region and femoral head tends to be closer to 40° when measured from the center of the femoral head in primates [46]. Selective Voronoi tessellation of more complex geometries,

such as this hypothetical example, would offer the potential to contour pore structures to follow trabecular orientation through the epiphyseal, metaphyseal, and diaphyseal portions of the long bones, providing a promising approach for generating femoral implants that mimic the natural femur. The vector field diagrams in this work show that preferential planes with a high seed density result in a co-oriented representative vector field within the implant struts. By controlling the rotation angle and spacing of adjacent seeding planes, the selective seeding approach introduced here offers an interesting alternative to contour local strut orientation along a complex mechanical axis while maintaining co-alignment with neighbouring struts and overall contiguity. As an example, Figure 8A shows the traditional implant geometry of a total hip joint replacement. Using conventionally repeated patterning (Figure 8B) fails to introduce local directionality into a curved implant geometry. Traditional Voronoi tessellation (Figure 8C) introduces a seemingly biomimetic structure but again lacks this degree of local trabecular alignment. However, selective Voronoi tessellation (Figure 8D) produces struts that are able to follow local contours of the implant while maintaining global anisotropy. Where this work demonstrates the relationship between seed density within the added seeding planes and resulting anisotropy, it is also possible to extend the method of selective Voronoi tessellation to produce isotropy-graded implants to best mimic the properties of existing human bone tissue in future work.
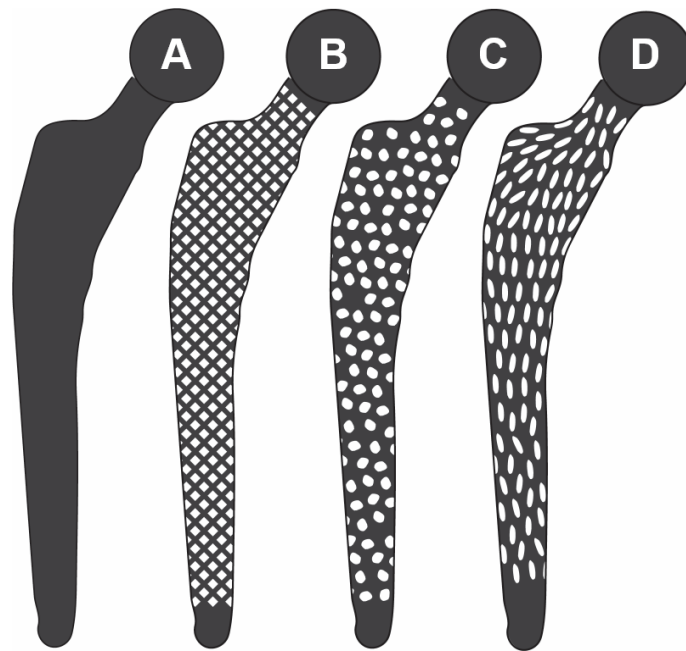
Figure 8: The use of porous structures in curved geometries such as the femoral component of hip implants. (A) The geometry of a traditional full-density implant. (B) The use of a reticulated porous geometry, where the use of a repeating pattern fails to follow contours anisotropy, (C) The use of standard Voronoi tessellation, where the implant geometry has a trabecular-like appearance, but struts do not follow the contoured geometry of the implant. (D) The use of selective Voronoi tessellation to form a biomimetic geometry, where struts are trabecular in appearance and follow the local contours of the implant.

5. Conclusions

This study demonstrates that selective Voronoi tessellation is an effective way to introduce global and local anisotropy into a biomimetic porous scaffold. Selective seed placement in the geometry results in preferential strut elongation. MIL measurements confirm that anisotropy increases when directionality is introduced into the scaffold compared to a standard Voronoi tessellation. Selective Voronoi tessellation also offers a way of elongating the struts along the mechanical axis in complex geometries without compromising the randomization of the structure. By introducing redistributed seeding planes, the anisotropy was increased to within the range of human trabecular bone without substantial compromise to the biomimetic inter-trabecular angle for 3N, 4N, and 5N junction types. 3N, 4N, and 5N angular distributions in all Voronoi implants were also observed to mimic trigonal planar, tetrahedral, and trigonal bipyramidal trabecular arrangements, respectively. This work paves a path towards the fabrication of customizable biomimetic implants using additive manufacturing with tunable mechanical properties based on the inherent bone geometry of a specific anatomical site in a patient. For example, this work shows that selective Voronoi tessellation can be used as an implant fabrication method for total hip arthroplasty to take into account the local anisotropic regions along the mechanical axis, where tunable degrees of seed density along preferred planes can add or subtract the desired quantity of anisotropy. For complex regions of bone associated with the replacement of the hip, such as the femoral metaphysis, selective Voronoi tessellation improves upon standard non-trabecular porous geometries. Future research should focus on modifying the selective Voronoi method to better match strut thickness in human trabeculae, characterizing the mechanical performance of these scaffolds, and investigating the *in vitro* and *in vivo* osseointegration potential of these geometries as biomimetic implants.

Acknowledgements

CRediT Authorship Statement

J. Deering: Conceptualization, Methodology, Software, Formal Analysis, Writing – Original Draft, Writing - Review & Editing

K.I. Dowling: Conceptualization, Methodology, Software, Formal Analysis, Writing – Original Draft, Writing – Review & Editing

L.A. DiCecco: Conceptualization, Software, Visualization, Writing - Review & Editing

G.D. McLean: Conceptualization, Investigation, Writing – Review and Editing

B. Yu: Conceptualization, Methodology, Writing – Review and Editing

K. Grandfield: Conceptualization, Supervision, Funding Acquisition, Writing – Review & Editing

References

1. Engh C, Bobyn J, Glassman A. Porous-coated hip replacement. The factors governing bone ingrowth, stress shielding, and clinical results. J Bone Jt Surg Br Volume. 1987;69-B(1):45–55.

2. Wik TS, Foss OA, Havik S, Persen L, Aamodt A, Witsø E. Periprosthetic fracture caused by stress shielding after implantation of a femoral condyle endoprosthesis in a transfemoral amputee—a case report. Acta Orthop. 2010;81(6):765–7.

3. Heinl P, Müller L, Körner C, Singer RF, Müller FA. Cellular Ti–6Al–4V structures with interconnected macro porosity for bone implants fabricated by selective electron beam melting. Acta Biomater. 2008;4(5):1536–44.

4. Karre R, Niranjan MK, Dey SR. First principles theoretical investigations of low Young's modulus beta Ti–Nb and Ti–Nb–Zr alloys compositions for biomedical applications. Mater Sci Eng C. 2015;50:52–8.

5. Harrysson OLA, Cansizoglu O, Marcellin-Little DJ, Cormier DR, West HA. Direct metal fabrication of titanium implants with tailored materials and mechanical properties using electron beam melting technology. Mater Sci Eng C. 2008;28(3):366–73.

6. Choren JA, Heinrich SM, Silver-Thorn MB. Young's modulus and volume porosity relationships for additive manufacturing applications. J Mater Sci. 2013;48(15):5103–12.

7. Bandyopadhyay A, Espana F, Balla VK, Bose S, Ohgami Y, Davies NM. Influence of porosity on mechanical properties and in vivo response of Ti6Al4V implants. Acta Biomater. 2010;6(4):1640–8.

8. de Vasconcellos LMR, Leite DO, de Oliveira FN, Carvalho YR, Cairo CAA. Evaluation of bone ingrowth into porous titanium implant: histomorphometric analysis in rabbits. Braz Oral Res. 2010;24(4):399–405.

9. Itälä AI, Ylänen HO, Ekholm C, Karlsson KH, Aro HT. Pore diameter of more than 100 μm is not requisite for bone ingrowth in rabbits. J Biomed Mater Res. 2001;58(6):679–83.

10. Li G, Wang L, Pan W, Yang F, Jiang W, Wu X, Kong X, Dai K, Hao Y. In vitro and in vivo study of additive manufactured porous Ti6Al4V scaffolds for repairing bone defects. Sci Rep-uk. 2016;6(1):34072.

11. Reznikov N, Chase H, Zvi YB, Tarle V, Singer M, Brumfeld V, Shahar R, Weiner S. Inter-trabecular angle: A parameter of trabecular bone architecture in the human proximal femur that reveals underlying topological motifs. Acta Biomater. 2016;44:65–72.

12. Sampath SA, Lewis S, Fosco M, Tigani D. Trabecular orientation in the human femur and tibia and the relationship with lower-limb alignment for patients with osteoarthritis of the knee. J Biomech. 2015;48(6):1214–8.

13. Rajpura A, Kendoff D, Board TN. The current state of bearing surfaces in total hip replacement. Bone Jt J. 2014;96-B(2):147–56.

14. Chevalier Y, Pahr D, Allmer H, Charlebois M, Zysset P. Validation of a voxel-based FE method for prediction of the uniaxial apparent modulus of human trabecular bone using macroscopic mechanical tests and nanoindentation. J Biomech. 2007;40(15):3333–40.

15. Helguero CG, Amaya JL, Komatsu DE, Pentyala S, Mustahsan V, Ramirez EA, Kao I. Trabecular Scaffolds' Mechanical Properties of Bone Reconstruction Using Biomimetic Implants. Proc Cirp. 2017;65:121–6.

16. Oftadeh R, Perez-Viloria M, Villa-Camacho JC, Vaziri A, Nazarian A. Biomechanics and Mechanobiology of Trabecular Bone: A Review. J Biomechanical Eng. 2015;137(1):010802.

17. Rudy DJ, Deuerling JM, Orías AAE, Roeder RK. Anatomic variation in the elastic inhomogeneity and anisotropy of human femoral cortical bone tissue is consistent across multiple donors. J Biomech. 2011;44(9):1817–20.

18. Enns-Bray WS, Owoc JS, Nishiyama KK, Boyd SK. Mapping anisotropy of the proximal femur for enhanced image based finite element analysis. J Biomech. 2014;47(13):3272–8.

19. Lin Y-H, Chang F-S, Chen K-H, Huang K-C, Su K-C. Mismatch between femur and tibia coronal alignment in the knee joint: classification of five lower limb types according to femoral and tibial mechanical alignment. Bmc Musculoskelet Di. 2018;19(1):411.

20. Cherian JJ, Kapadia BH, Banerjee S, Jauregui JJ, Issa K, Mont MA. Mechanical, Anatomical, and Kinematic Axis in TKA: Concepts and Practical Applications. Curr Rev Musculoskelet Medicine. 2014;7(2):89–95.

21. Hernigou P, Medevielle D, Debeyre J, Goutallier D. Proximal tibial osteotomy for osteoarthritis with varus deformity. A ten to thirteen-year follow-up study. J Bone Jt Surg. 1987;69(3):332–54.

22. Sikorski JM. Alignment in total knee replacement. Bone Joint J. 2008;90-B(9):1121–7.

23. Fantini M, Curto M, Crescenzio FD. A method to design biomimetic scaffolds for bone tissue engineering based on Voronoi lattices. Virtual Phys Prototyp. 2016;11(2):77–90.

24. Ying S, Xu G, Li C, Mao Z. Point Cluster Analysis Using a 3D Voronoi Diagram with Applications in Point Cloud Segmentation. Isprs Int Geo-inf. 2015;4(3):1480–99.

25. Silva MJ, Hayes WC, Gibson LJ. The effects of non-periodic microstructure on the elastic properties of two-dimensional cellular solids. Int J Mech Sci. 1995;37(11):1161–77.

26. Alkhader M, Vural M. Mechanical response of cellular solids: Role of cellular topology and microstructural irregularity. Int J Eng Sci. 2008;46(10):1035–51.

27. Zhu HX, Hobdell JR, Windle AH. Effects of cell irregularity on the elastic properties of 2D Voronoi honeycombs. J Mech Phys Solids. 2001;49(4):857–70.

28. Seiler PE, Tankasala HC, Fleck NA. The role of defects in dictating the strength of brittle honeycombs made by rapid prototyping. Acta Mater. 2019;171:190–200.

29. Latture RM, Begley MR, Zok FW. Defect Sensitivity of Truss Strength. J Mech Phys Solids. 2019;124:489–504.

30. Pham M-S, Liu C, Todd I, Lertthanasarn J. Damage-tolerant architected materials inspired by crystal microstructure. Nature. 2019;565(7739):305–11.

31. Maconachie T, Leary M, Lozanovski B, Zhang X, Qian M, Faruque O, Brandt M. SLM lattice structures: Properties, performance, applications and challenges. Mater Design. 2019;183:108137.

32. Gebhardt A. Understanding Additive Manufacturing. Munich: Carl Hanser Verlag; 2011.

33. Wang X, Xu S, Zhou S, Xu W, Leary M, Choong P, Qian M, Brandt M, Xie YM. Topological design and additive manufacturing of porous metals for bone scaffolds and orthopaedic implants: A review. Biomaterials. 2016;83:127–41.

34. Kruth J, Mercelis P, Vaerenbergh JV, Froyen L, Rombouts M. Binding mechanisms in selective laser sintering and selective laser melting. Rapid Prototyping J. 2005;Volume 11(Issue 1):26–36.

35. Zheng Q, Ju S, Jiang D. Anisotropic mechanical properties of diamond lattice composites structures. Compos Struct. 2014;109:23–30.

36. Liang H, Yang Y, Xie D, Li L, Mao N, Wang C, Tian Z, Jiang Q, Shen L. Trabecular-like Ti-6Al-4V scaffolds for orthopedic: fabrication by selective laser melting and in vitro biocompatibility. J Mater Sci Technol. 2019;35(Der Unfallchirurg 109 2006):1284–97.

37. Fantini M, Curto M. Interactive design and manufacturing of a Voronoi-based biomimetic bone scaffold for morphological characterization. Int J Interact Des Manuf Ijidem. 2018;12(2):585–96.

38. Smit TH, Schneider E, Odgaard A. Star length distribution: a volume-based concept for the characterization of structural anisotropy. J Microsc-oxford. 1998;191(3):249–57.

39. Whitehouse WJ. The quantitative morphology of anisotropic trabecular bone. J Microsc-oxford. 1974;101(2):153–68.

40. Reznikov N, Alsheghri AA, Piché N, Gendron M, Desrosiers C, Morozova I, Siles JMS, Gonzalez-Quevedo D, Tamimi I, Song J, Tamimi F. Altered topological blueprint of trabecular bone associates with skeletal pathology in humans. Bone Reports. 2020;12:100264.

41. Odgaard A. Three-dimensional methods for quantification of cancellous bone architecture. Bone. 1997;20(4):315–28.

42. Doershuk LJ, Saers JPP, Shaw CN, Jashashvili T, Carlson KJ, Stock JT, Ryan TM. Complex variation of trabecular bone structure in the proximal humerus and femur of five modern human populations. Am J Phys Anthropol. 2019;168(1):104–18.

43. Parkinson IH, Fazzalari NL. Interrelationships Between Structural Parameters of Cancellous Bone Reveal Accelerated Structural Change at Low Bone Volume. J Bone Miner Res. 2003;18(12):2200–5.

44. Greenwood C, Clement JG, Dicken AJ, Evans JPO, Lyburn ID, Martin RM, Rogers KD, Stone N, Adams G, Zioupos P. The micro-architecture of human cancellous bone from fracture neck of femur patients in relation to the structural integrity and fracture toughness of the tissue. Bone Reports. 2015;3:67–75.

45. Clohisy JC, Nunley RM, Carlisle JC, Schoenecker PL. Incidence and Characteristics of Femoral Deformities in the Dysplastic Hip. Clin Orthop Relat R. 2009;467(1):128–34.

46. Ryan TM, Ketcham RA. Angular orientation of trabecular bone in the femoral head and its relationship to hip joint loads in leaping primates. J Morphol. 2005;265(3):249–63.

Selective Voronoi Tessellation as a Method to Design Anisotropic and Biomimetic Implants

Joseph Deering [a, †], Kierdra I. Dowling [a, †], Liza-Anastasia DiCecco [a], Griffin D. McLean [b], Bosco Yu [a], Kathryn Grandfield [a,c,*]

[†] *These authors contributed equally.*
[a] *Department of Materials Science and Engineering, McMaster University, Hamilton, ON, Canada*
[b] *Department of Mechanical Engineering, McMaster University, Hamilton, ON, Canada*
[c] *School of Biomedical Engineering, McMaster University, Hamilton, ON, Canada*

The link to Grasshopper scripts and STL files for the isotropic, 3-5 SPP, 5-7 SPP, and 8-10 SPP implant structures can be found below. The Grasshopper plug-in for Rhino 6 modelling software is required to run the scripts, but STL files can be opened with any modelling software.
https://github.com/j-deering/Anisotropic-Implants-by-Voronoi-Tessellation